Chemical Science

ROYAL SOCIETY OF CHEMISTRY

EDGE ARTICLE

View Article Online
View Journal | View Issue

Cite this: *Chem. Sci.*, 2025, **16**, 11138

All publication charges for this article have been paid for by the Royal Society of Chemistry

Two-sided asymmetric nanofluidic membrane for enhanced ion transport and osmotic energy harvesting†

Qijun Zheng,[a] Yue Shen,[a] Junjian Lu,[a] Yan Xu,[b] Xing-Hua Xia[c] and Chen Wang *[a]

Received 17th February 2025
Accepted 9th May 2025

DOI: 10.1039/d5sc01237f

rsc.li/chemical-science

Nanofluidic membranes hold great potential for osmotic energy conversion. Creating high-efficiency ion-permselective membranes with well-fit channel structures continues to pose a persistent challenge. In this work, we design a novel dual asymmetric nanofluidic membrane with MXene and Nafion separately on the two sides of anodic aluminum oxide (AAO) for enhanced ion selective transport. Driven by osmosis, cations are initially separated by the Nafion layer with abundant negative charges, then followed by accelerated transport due to the interface potential abruptness between AAO channels and the MXene layer. Following that, the MXene layer acts as the second cation selective layer to further achieve ion charge separation. Benefiting from the dual ion selectivity and accelerated ion transfer, a high cation transfer number of 0.95 can be realized using the present membrane. In addition, the photothermal property of MXene could generate an additional thermal gradient under light irradiation, further promoting ion transfer. Taking advantage of the present two-sided asymmetric nanofluidic membrane, the output power could be up to 65.6 W m^{-2} at 500-fold NaCl salinity gradient, which is much higher than that of the majority of previously reported reverse electrodialysis membranes (3.0–35.0 W m^{-2}). The present work opens up a new strategy for constructing novel asymmetric nanofluidic devices for enhanced ion transport and osmotic energy harvesting.

Introduction

The growing global energy demand has sparked heightened interest in the advancement of clean energy. Osmotic energy, an environmentally benign form of blue energy harnessed from differential salt concentration solutions, has attracted considerable attention due to its potential to mitigate the adverse environmental impacts of traditional energy.[1,2] Reverse electrodialysis (RED) technology has emerged as one of the most promising methods to harness this energy, enabling the direct conversion of salinity gradients into electricity through facilitating the directional movement of charges across permselective membranes.[3] Currently, advanced nanomaterials such as covalent organic frameworks,[4] metal organic frameworks,[5,6] graphene oxide,[7,8] and black phosphorus have been employed as permselective membranes for osmotic energy harvesting.[9] Although these findings undoubtedly offer novel inspiration for osmotic energy harvesting technologies, the achieved output power densities generally remain below 12 W m^{-2}, primarily due to the inadequate permselectivity of membranes. Several improvements have been performed to enhance ion selectivity through surface coating,[10] introducing surface functional groups,[11] or modifying the phase structure of nanomaterials.[12] Despite these advancements, effective constructing strategies to enhance the permselectivity of nanofluidic membranes remain to be explored.

Asymmetric nanofluidic membranes are usually composed of two or more different nanomaterials, integrating unique properties of different materials.[13–16] From a structural perspective, asymmetric nanofluidic membranes exhibit diverse pore architectures achieved by integrating multi-channels with distinct spatial arrangements, structures and pore sizes.[17–19] The structural characteristics enable more functions for diverse ion transport and hold paramount significance for further applications such as ion sieving, water purification, and energy conversion.[20–22] Recently, we developed an asymmetric plasmonic electron sponge membrane for enhanced ion selective transport.[23] The inherent structural asymmetry and higher charge density of the prepared nanofluidic membrane ensure enhanced interfacial transport resulting in a corresponding cation transfer number of PESM that can reach as high as 0.83. In another example, an

[a]Jiangsu Collaborative Innovation Center of Biomedical Functional Materials, Jiangsu Key Laboratory of New Power Batteries, School of Chemistry and Materials Science, Nanjing Normal University, Nanjing 210023, China. E-mail: wangchen@njnu.edu.cn
[b]Department of Chemical Engineering, Graduate School of Engineering, Osaka Prefecture University, Sakai, Osaka 599-8570, Japan
[c]State Key Laboratory of Analytical Chemistry for Life Science, School of Chemistry and Chemical Engineering, Nanjing University, Nanjing 210023, China

† Electronic supplementary information (ESI) available. See DOI: https://doi.org/10.1039/d5sc01237f

asymmetric branched alumina membrane with large geometric gradient and high charge density was developed. Ultrafast ion transport and outstanding cation selectivity enabled it to achieve an output power of up to 8 W m^{-2}.[24] Although the aforementioned asymmetric nanofluidic membranes demonstrate satisfactory performance, the single-level asymmetric architecture inevitably compromises both ion selectivity and energy conversion efficiency. Recently, a unique multi-level asymmetric heterogeneous membrane was designed for high-efficiency water purification.[25] The two functional materials on both sides of the membrane can be used to construct a multi-adsorption interface, capable of simultaneously removing several types of organic micropollutants. Consequently, high flux and efficient separation of contaminants have been successfully achieved, with a separation efficiency of approximately 100%. It is highly expected that multi-level asymmetric nanofluidic membranes would have great potential for efficient osmotic energy harvesting through synergistic material optimization coupled with multi-ion selective layer integration.

Inspired by the above outstanding work, herein, we developed a two-sided asymmetric nanofluidic membrane composed of MXene/anodic aluminum oxide/Nafion (MXene/AAO/Nafion) for enhanced ion selective transport and efficient osmotic energy harvesting (Scheme 1A). Two functional layers with abundant negative surface charges on both sides of the asymmetric membrane help to construct dual ion selective interfaces. When separated by the MXene/AAO/Nafion membrane, ions are driven by a salinity gradient from high to low concentration. Specific charges in the functional layers attract ions into nanochannels, forming an electrical double layer (EDL) and realizing rapid directional migration.[26] The cations are initially rapidly separated in the Nafion layer during the transmembrane diffusion, then followed by accelerated transport due to the interface potential abruptness between AAO channels and the MXene layer. As a result, the dual ion selective layers and accelerated ion transfer resulted in both high ion selectivity and permeability. Additionally, benefiting from the remarkable photothermal conversion efficiency of MXene, a temperature gradient is generated simultaneously, resulting in light-driven directional ion migration. By integrating solar energy with a salinity gradient, the driving force for nanofluidic ion transportation is reinforced, leading to significant enhancements in osmotic energy harvesting (Scheme 1B). Under a 0.01/5 M NaCl concentration gradient, the maximum power density of the MXene/AAO/Nafion membrane increased from the initial 47.8 W m^{-2} to 65.6 W m^{-2} with light irradiation, surpassing that of the majority of previously reported RED membranes (3.0–35.0 W m^{-2}). This study integrates the structural benefits of asymmetric membranes with concentration-driven and light-driven processes, providing an ideal strategy for high ion selectivity and permeability towards high-efficiency osmotic energy harvesting.

Results and discussion

Fabrication and characterization of MXene/AAO/Nafion

The two-sided asymmetric nanofluidic membrane was fabricated by integrating MXene and Nafion into the two sides of AAO. Firstly, AAO was fabricated using the anodization oxidation technique.[22] The diameter of each of the fabricated AAO array channels is about 50 nm (Fig. S1 and S2†). The prepared MXene nanosheet suspension was fixed on one side of AAO by vacuum-assisted filtration. Subsequently, the other side of the membrane was spin-coated with ionomer Nafion. The morphology of the two-sided asymmetric MXene/AAO/Nafion membrane was characterized by scanning electron microscopy (SEM) (Fig. 1A). The MXene layer on the surface of the AAO membrane appears to be uniform and dense, exhibiting a typical lamellar structure, and the thickness is approximately 182 nm (Fig. 1B and C). Surface energy-dispersive X-ray spectroscopy (EDX) mapping presents the characteristic signals of C, F and Ti elements in the MXene layer (Fig. 1D). The dense Nafion layer was deposited on the other side of the AAO membrane, and the thickness is approximately 97 nm (Fig. 1E and F). Surface EDX mapping presents the characteristic signals of C, F and S elements in the Nafion layer (Fig. 1G). The results obtained confirm the presence of a two-sided asymmetric structure on the AAO substrate.

The structures of the MXene and Nafion layers were further characterized. A mild etching method was used to selectively etch the bulk Ti_3AlC_2 phase to obtain few-layered $Ti_3C_2T_x$ nanosheets (Fig. S3†). The disappearance of the (008) diffraction peak at 39° in the X-ray diffraction (XRD) pattern of $Ti_3C_2T_x$, with the (002) peak undergoing a leftward shift, indicates successful etching of the Al layer (Fig. 1H). The (002) peak of MXene appears at 5.68°, corresponding to a *d*-spacing of 1.56 nm as calculated by Bragg's law. Given that the theoretical thickness of an MXene nanosheet is 0.98 nm, the effective interfacial height is approximately 0.58 nm.[27,28] The transmission electron microscopy results indicate that the lateral size of the prepared single-layer MXene nanosheet is approximately 1 μm. The high aspect ratio is in favor of the construction of a uniform and ordered layer nanochannel (Fig. S4 and S5†). Subsequently, chemical characterization was conducted. In the X-ray photoelectron spectroscopy (XPS) analysis, three C 1s peaks located at 286.10, 282.0 and 284.8 eV corresponded to $Ti_3C_2T_x$ and can be assigned to the C–O, C–Ti, and C–C bonds (Fig. S6†). The Fourier transform infrared (FTIR) spectrum of $Ti_3C_2T_x$ exhibits characteristic peaks at 3461 cm^{-1} and 1635 cm^{-1}, corresponding to the O–H bond and C=O bond, respectively (Fig. 1I). The abundant surface functional groups facilitate hydrogen bonding with hydroxyl groups on AAO, thereby enhancing the interfacial interaction between MXene and AAO (Fig. S7†). For Nafion, the obvious signals at 1135 cm^{-1} and 1085 cm^{-1} are attributed to sulfonate groups (Fig. 1J). Additionally, the pore size of the Nafion membrane is approximately 2.5 nm.[29] Furthermore, comparative zeta-potential measurements reveal that $Ti_3C_2T_x$ demonstrates a more negative surface charge (−34.49 mV) than Nafion (−25.04 mV), indicating an asymmetrical charge of the two sides of the MXene/AAO/Nafion membrane (Fig. 1K and S8, S9†). The contact angles of the MXene and Nafion layers are determined to be 65.5° and 88.2°, respectively (Fig. S10†). The high electronegativity and hydrophilicity of the MXene layer and Nafion layer can improve ion entry and transportation.

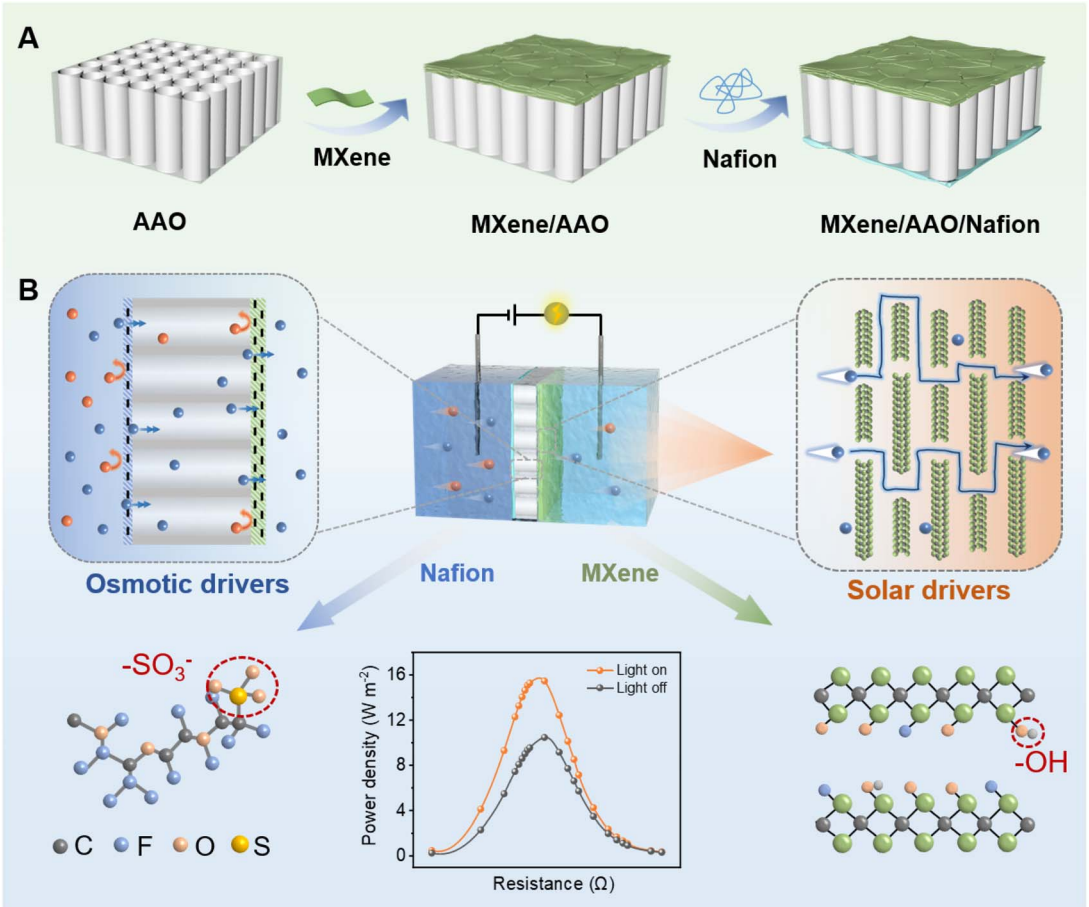

Scheme 1 Schematic illustration of the two-sided asymmetric MXene/AAO/Nafion membrane for osmotic energy harvesting. (A) Fabrication process of the MXene/AAO/Nafion membrane. (B) High-efficiency osmotic energy harvesting using the two-sided asymmetric MXene/AAO/Nafion membrane. Orange and blue arrows indicate the transport directions of anions and cations, respectively.

Enhanced ion permeation

In order to systematically investigate the transmembrane ion transport behavior, the MXene/AAO/Nafion membrane was assembled into a custom electrochemical cell (Ag/AgCl electrodes) for real-time ion current monitoring (Fig. 2A and S11, S12†). The standard electrolyte chosen was potassium chloride (KCl) due to the similar ion mobilities and diffusion coefficients of K^+ and Cl^-. Current–voltage (*I–V*) tests were conducted at various KCl concentrations within the voltage range of −1 to +1 V. As shown in Fig. 2B, the ion transport of the membrane exhibits a slightly diode-like behavior. For the membrane with only MXene or Nafion deposited on one side of AAO (defined as MXene/AAO and Nafion/AAO), the diode-like ion transport is more obvious (Fig. S13 and S14†). The reason for this phenomenon is that both sides of the MXene/AAO/Nafion membrane contain negatively charged materials, reducing the charge asymmetry of the whole membrane.[30] Then, the ion transport stability across the MXene/AAO/Nafion membrane was evaluated by a current–time (*I–T*) test, involving alternating application of an external bias voltage of +1 V and −1 V (Fig. 2C). Each test cycle was conducted in 0.1 M KCl solution for 10 min. As shown, the ion transport maintains a very good stability, as evidenced by the currents remaining basically constant under both positive and negative bias. The ion conductance of the membrane in electrolyte with varying concentrations was determined from the *I–V* curve in Fig. 2D. When the electrolyte concentration is below 0.1 M, the transmembrane conductance significantly deviates from the bulk value, demonstrating that ion transport becomes predominantly governed by the surface charge of the nanofluidic membrane.

To assess the surface charge-controlled ion transport, 0.01 M KCl solution was selected to examine the ion current of diverse membranes (ensuring sufficient overlap of EDL). In this condition, the ion concentration within the nanochannels is governed by the negatively charged material layers. As illustrated in Fig. 2E, the two-sided asymmetric MXene/AAO/Nafion membrane displayed larger current responses compared to the MXene/AAO membrane and Nafion/AAO membrane. More hydrophilic nanochannels typically lead to a reduction in ion transport resistance, thereby resulting in higher conductivity for MXene/AAO compared to Nafion/AAO. After coupling MXene and Nafion, the conductance of the two-sided asymmetric MXene/AAO/Nafion membrane increases up to 36.98 μS at +1 V, surpassing that of the other two membranes (Fig. 2F). The larger ion conductance is attributed to the high charge accumulation of the MXene/AAO/Nafion membrane. The dual

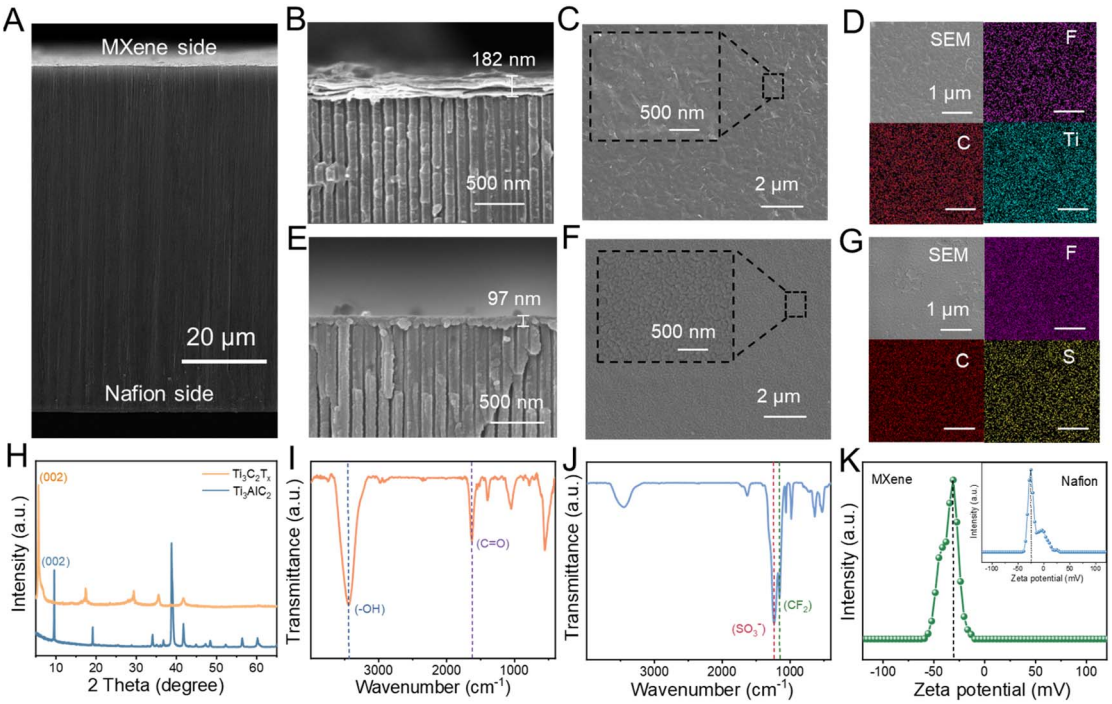

Fig. 1 Characterizations of the two-sided asymmetric MXene/AAO/Nafion membrane. (A) Cross-sectional image of MXene/AAO/Nafion. (B) Cross-sectional image of MXene layer. (C and D) Surface image of MXene layer and EDX elemental mappings. (E) Cross-sectional image of Nafion layer. (F and G) Surface image of Nafion layer and EDX elemental mappings. (H) Powder XRD patterns of Ti_3AlC_2 and $Ti_3C_2T_x$. (I) FTIR spectrum of $Ti_3C_2T_x$. (J) FTIR spectrum of Nafion. (K) Zeta potential of MXene and Nafion.

functional layer of MXene/AAO/Nafion enhances carrier concentration through its negatively charged properties, thereby improving electrical conductivity.[30,31]

Enhanced ion selectivity

The ion selectivity of the MXene/AAO/Nafion membrane was evaluated using an electrochemical approach. 1 M KCl solution was introduced on the Nafion side and 1 μM KCl solution was

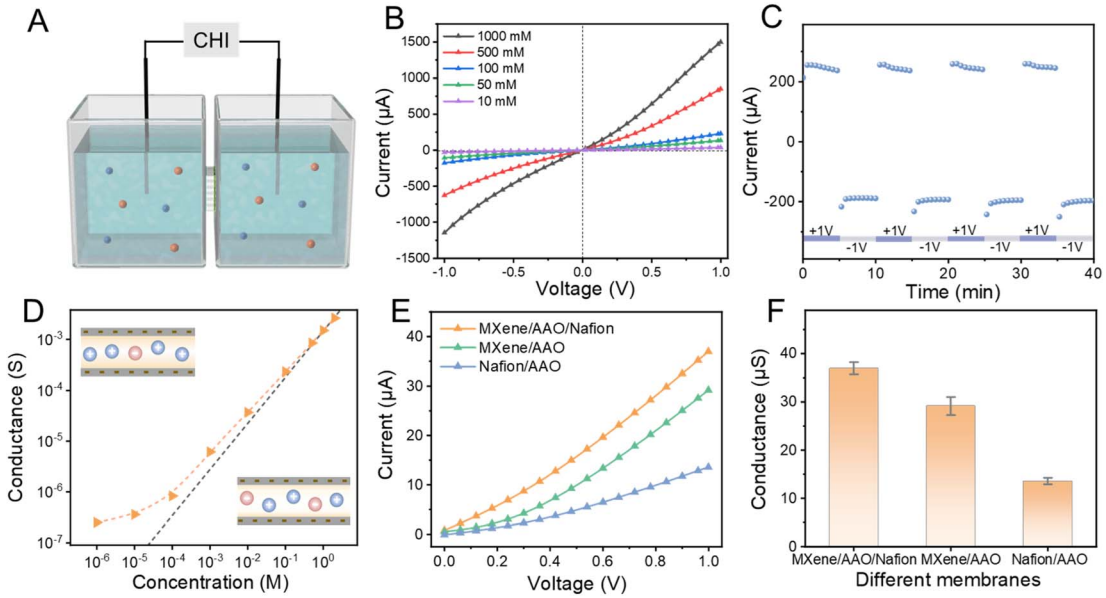

Fig. 2 Enhanced ion permeation. (A) Schematic of the custom electrochemical cell for testing ion transport. (B) *I*–*V* curves of the MXene/AAO/Nafion membrane in KCl solutions of varying concentrations. (C) *I*–*T* curves of the MXene/AAO/Nafion membrane in 0.1 M KCl solution under an alternating external bias voltage of +1 V and −1 V. (D) Ion conductance of the MXene/AAO/Nafion membrane in KCl solutions of varying concentrations. (E) *I*–*V* curves and (F) ion conductance of diverse membranes in 0.01 M KCl.

introduced on the MXene side. Due to the substantial concentration gradient between the two solutions, the ion current was predominantly driven by transport from the high-concentration (C_H, 1 M) side to the low-concentration (C_L, 1 μM) side. When the anode was positioned on the C_H side, ion current was predominantly contributed by K^+ ions. Similarly, when the anode was positioned on the C_L side, the Cl^- ions predominantly contributed to the ion current. Obviously, the K^+ current surpasses that of Cl^-, indicating that the MXene/AAO/Nafion membrane displays excellent cation selectivity (Fig. 3A and S15†). Similarly, the MXene/AAO membrane and the Nafion/AAO membrane also exhibit cation selectivity under concentration gradients (Fig. S16 and S17†). However, the K^+ currents of both the MXene/AAO and the Nafion/AAO membranes are lower than that of the MXene/AAO/Nafion membrane. This phenomenon may arise from the limited selectivity of the single-level asymmetric structure. Afterwards, the effect of the two-sided asymmetric structure on selective cation transport was further investigated.

By creating a concentration gradient across the membrane, cations are able to selectively cross the membrane and generate potential differences. The intercepts of the *I–V* curve on the voltage and current axes are denoted as open-circuit voltage (V_{OC}) and short-circuit current (I_{SC}), respectively (Fig. 3B). Notably, the obtained V_{OC} consists of two sections: the diffusion potential (E_{diff}) and the redox potential (E_{redox}). E_{diff} is caused by the salinity gradient across the membrane, while E_{redox} is produced by the voltage drop on the interface of the electrode and electrolyte (Fig. S18†). When the NaCl concentration on the MXene side was 0.5 M and on the Nafion side was 0.01 M, V_{OC} and I_{SC} were measured as 104 mV and 4.736 μA respectively. V_{OC} increased to 154 mV and I_{SC} increased to 10.64 μA when the concentration gradient was reversed. This phenomenon may arise from the transmembrane potential difference generated between Nafion and MXene due to their charge asymmetry, which is directed from the Nafion side to the MXene side.[21] When 0.5 M NaCl is placed on the Nafion side, the concentration gradient drives cations to migrate from Nafion to MXene. This diffusion direction aligns with the internal electric field, thereby enhancing ion transport. Conversely, when the concentration gradient is reversed, ion transport would be suppressed, resulting in lower V_{OC} and I_{SC} values. Consequently, in order to achieve a high diffusion potential, all subsequent experiments were conducted by filling the MXene side with a low-concentration solution. Fig. 3C clearly reveals that the establishment of the two-sided asymmetric structure not only enhances the ion selectivity (resulting in an increase in V_{OC}) but also improves the ion permeation (leading to an increase in I_{SC}). The mechanism for enhanced ion selectivity is schematically shown in Fig. 3D. Compared to the MXene/AAO and Nafion/AAO membranes, the two functional layers on both sides of the asymmetric membrane realize a dual ion separation, thus further enhancing the cation selectivity. Specifically, the ion transport in nanochannels is mainly controlled by surface charge.[24] Specific surface charges in the selective layer will attract ions into nanochannels, forming an EDL and realizing rapid directional migration.[26,32,33] Driven by the concentration gradient, cations are initially separated in the Nafion layer with abundant negative charges, then followed by accelerated transport by the interface potential abruptness between AAO channels and the MXene layer. Meanwhile, the MXene layer acts as the second cation selective layer, further achieving ion charge separation.

With a fixed KCl concentration of 1 mM on the MXene side and varying KCl concentration from 1 mM to 1 M on the Nafion side, both E_{diff} and I_{SC} values increase with the salinity gradient (Fig. 3E, S19 and Table S1†). The E_{diff} and I_{SC} values of MXene/AAO and Nafion/AAO also increase with the concentration gradient (Fig. S20†). Notably, the the cation transference number (t_+) value of the MXene/AAO/Nafion membrane exhibits the highest performance across various salinity gradients compared to the single-level asymmetric membranes (Fig. 3F). In previous studies, the selectivity of nanofluidic membranes in high-salinity environments was generally diminished due to the reduced thickness of the EDL and limited electrostatic effects (Table S2†).[23,34] However, the t_+ value of the MXene/AAO/Nafion membrane remains steady at 0.9, even when the electrolyte solution on the high-concentration side reached 1 M (Fig. 3F). This remarkable performance stems from the integration of MXene and Nafion, which creates synergistic effects between dual ion selective layers, thereby preserving outstanding cation selectivity under high-salinity conditions. Furthermore, the MXene/AAO/Nafion membrane exhibits a t_+ value of 0.95 in an artificial seawater/river water system, which is better than the performance of most previously reported nanofluidic membranes (Fig. 3G, H and Tables S3, S4†).

On this basis, the application potential of the present two-sided asymmetric membrane was investigated for osmotic energy harvesting. The osmotic energy harvested from the MXene/AAO/Nafion membrane was quantified by connecting an external resistor (R_L). The output power density (P) can be calculated as $P = I^2 \times R_L/S$. As shown in Fig. S21,† the current density decreases with increasing load resistance, while the maximum output power is achieved at an intermediate resistance of 20 kΩ. The MXene/AAO/Nafion membrane delivers an output power density of 10.4 W m^{-2} at a 0.01/0.5 M NaCl concentration gradient, surpassing that of both the MXene/AAO and Nafion/AAO membranes. Meanwhile, the MXene/AAO/Nafion membrane also demonstrates significantly higher power density compared to both MXene/AAO/MXene and Nafion/AAO/Nafion membranes (Fig. S22†). The outstanding performance can be attributed to the fact that the MXene/AAO/Nafion membrane not only enables dual ion separation, but its asymmetric charge distribution also effectively suppresses ion concentration polarization (ICP), thereby further enhancing osmotic energy harvesting.[35,36] In addition, considering that a greater thickness would lead to a weakened ion permeability, the MXene/AAO/Nafion membrane with an MXene layer of ~182 nm and Nafion layer of ~97 nm was adopted in the following experiments (Fig. S23–S26†).

Light-stimulated ion transport

To investigate the ion transport behavior of the MXene/AAO/Nafion membrane under light stimulation, we integrated

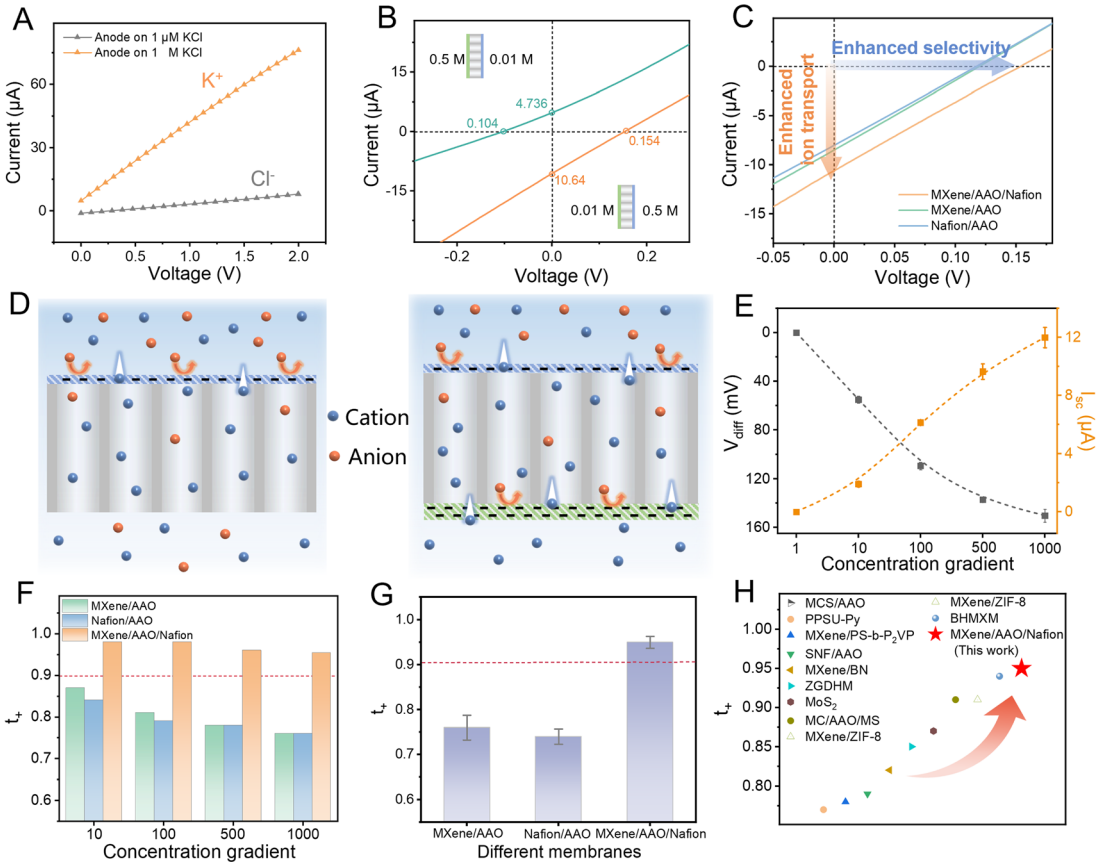

Fig. 3 Excellent cation selectivity. (A) *I*–*V* curves of the MXene/AAO/Nafion membrane in two different salt concentrations. The gray curve and orange curve represent the current contributed by Cl^- and K^+, respectively. (B) *I*–*V* curves of the MXene/AAO/Nafion membrane recorded at a 0.01/0.5 M NaCl concentration gradient. The green curve depicts a higher concentration on the MXene side, whereas the orange curve depicts a higher concentration on the Nafion side. (C) *I*–*V* curves of the MXene/AAO, Nafion/AAO and MXene/AAO/Nafion membranes at a 0.01/0.5 M NaCl concentration gradient. (D) Schematic diagram of enhanced cation selectivity of two-sided asymmetric structure. (E) I_{SC} and E_{diff} at a range of KCl salinity gradients. MXene side was in contact with 1 mM KCl, while the KCl concentration on Nafion side was progressively increased from 1 mM to 1 M. (F) The cation transference number of the MXene/AAO, Nafion/AAO and MXene/AAO/Nafion membranes at a range of KCl salinity gradients and (G) at a 0.01/0.5 M NaCl concentration gradient. (H) Comparison of the cation transference number with that of previously reported devices at a 0.01/0.5 M NaCl concentration gradient.

a xenon lamp into the nanofluidic system as an illuminating source (Fig. 4A). When the electrochemical cells were filled with the same concentration of KCl solutions, no distinct ion current was observed without illumination. However, when one side was exposed to light irradiation, we noticed a remarkable increase in ion current, peaking at approximately −130 nA within 80 s. When the light was off, the current quickly reverted to its initial state, implying the observed current was induced by light (Fig. 4B and S27†). To explore the fundamental mechanism of light-induced ion transport, we employed an infrared thermographic camera to observe the temperature variations of the MXene/AAO/Nafion membrane before and following illumination (Fig. 4C). The result demonstrates the excellent photothermal conversion performance of the MXene/AAO/Nafion membrane, as evidenced by a rapid temperature increase from 25 °C to approximately 65 °C within just 60 s of illumination (Fig. S28†). The temperature of the MXene/AAO membrane can reach up to 60 °C under the same light intensity (Fig. S29†). However, the temperature of the Nafion/AAO membrane is maintained at around 33 °C (Fig. S30†). In addition, MXene dispersions show efficient light absorption in the ultraviolet-visible spectrum (Fig. S31†). Upon light irradiation, the MXene/AAO/Nafion membrane elevated the localized solution temperature from 24.9 °C to 41.3 °C, further confirming its efficient photothermal conversion capability (Fig. S32†). Meanwhile, when a 0.1 V external voltage was imposed on the different membranes, the currents of the MXene/AAO and MXene/AAO/Nafion membranes sharply increased with illumination (Fig. S33†). Interestingly, the currents could also be enhanced by increasing the light intensity (Fig. S34†). Based on the analysis provided above, it can be argued that the MXene layer has an excellent photothermal conversion performance.

From a thermodynamic perspective, the Gibbs free energy of the solution near the illuminated region decreases as the temperature rises. Consequently, the spontaneous diffusion of ions tends to occur in the direction of decreasing Gibbs free energy, leading to an opposite direction of ion transport compared to the temperature gradient.[36–38] In order to verify

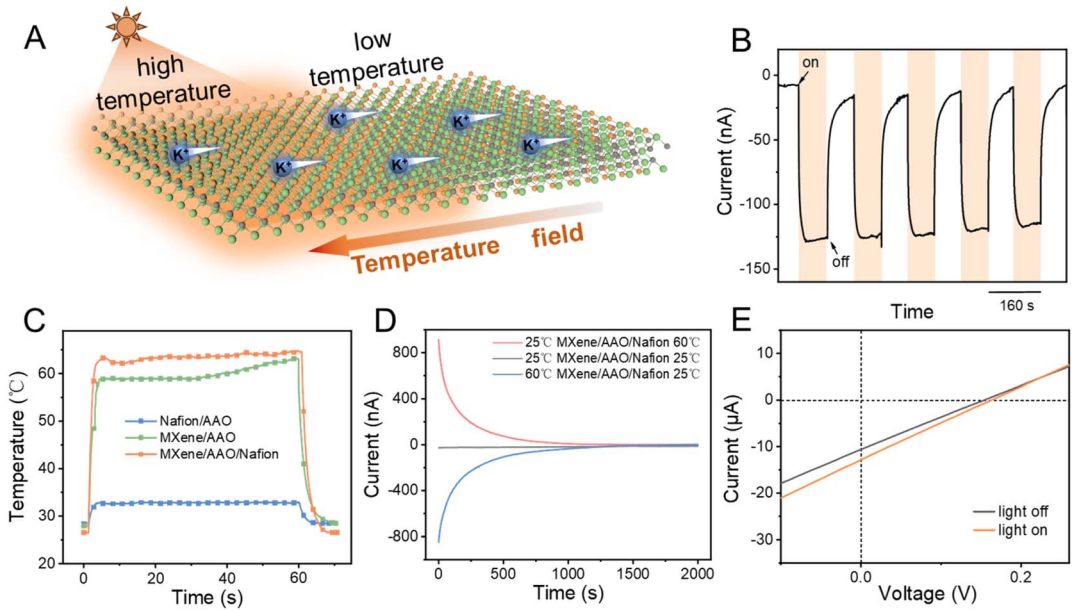

Fig. 4 Photo-stimulated ion transport. (A) Scheme of ion transport under solar irradiation. (B) Photocurrent through MXene/AAO/Nafion under irradiation (0.01 M KCl). (C) Time-dependent temperature change for MXene/AAO, Nafion/AAO and MXene/AAO/Nafion. (D) Photothermal effect simulation. (E) *I*–*V* curves of the MXene/AAO/Nafion membrane with and without light irradiation at a 0.01/0.5 M NaCl concentration gradient.

that the light-induced ion current was driven by the temperature gradient, parallel experiments were also conducted. Specifically, two cells were filled with a 65 °C KCl solution and a room-temperature KCl solution, respectively, to simulate the photothermal experimental conditions. As shown in Fig. 4D, when the temperature on both sides of the MXene/AAO/Nafion membrane was equal, there was no discernible ion current. However, once the temperature difference was established between the two-sided solutions, an evident current arose in the opposite direction to the temperature gradient, suggesting that the ions flowed from the lower to higher temperature region. When the temperature difference between the two-sided solutions gradually decreased, the corresponding ion current also gradually decreased. The results show that the magnitude and direction of the light-induced ion current are determined by the temperature difference.

Afterwards, the influence of light direction on the performance of ion transport was further investigated. We incorporated illumination into an artificial seawater/river water system. The increase of the temperature near the membrane caused by illumination on the low-concentration side was found to restrict the expansion of the ICP zone,[35] which enabled the realization of an effective concentration gradient (Fig. S35†). Additionally, when the low-concentration side was exposed to illumination, the direction of concentration-driven ion transport coincided with that of light-driven ion transport,[14,39] leading to a noticeable increase in the osmotic current and the value of t_+ also increased from 0.95 to 0.99 (Fig. 4E and S36†). However, when the high-concentration side was exposed to illumination, the direction of ion transport driven by light is opposite to that driven by concentration gradients, and a decrease in the osmotic current value was found (Fig. S37†). The above results demonstrate that the light-induced selective ion transport behavior influenced by illumination is also related to light direction. Therefore, in order to obtain the best driving force, the light irradiation was placed on the low-concentration side in the subsequent experiments. In addition, we also explored the possibility of energy conversion solely under light irradiation, without the presence of salinity gradients. By connecting an external resistor, the maximum ion power density value obtained is about 11.8 mW m^{-2} (Fig. S38†). This result shows that the ion energy can be harnessed in a solution of the same concentration, which greatly expanded the application range of ion energy harvesting.

Light-enhanced osmotic energy harvesting

As expected, by integrating both light-driven and concentration-driven mechanisms, an excellent osmotic energy harvesting performance could be achieved using the present MXene/AAO/Nafion membrane (Fig. 5A). Under light irradiation, the output power in a 0.01/0.5 M NaCl concentration gradient increased from the initial 10.4 W m^{-2} to 15.2 W m^{-2}, representing a 46% enhancement compared to dark conditions (Fig. 5B, S39†). Notably, the output power of MXene/AAO/Nafion is also obviously higher than that of AAO, MXene/AAO and Nafion/AAO under illumination (Fig. S40–S43†), which can be ascribed to the optimized structure design. To explore the ability of MXene/AAO/Nafion in high-salinity environments, we evaluated its power density by maintaining a low concentration of 0.01 M and adjusting the high concentration within a range of 0.05 to 5 M. Notably, the output power can reach a maximum of 65.6 W m^{-2} at a 500-fold NaCl salinity gradient and 59.6 W m^{-2} at a 300-fold KCl salinity gradient under illumination, indicating that MXene/AAO/Nafion still has good stability and performance in

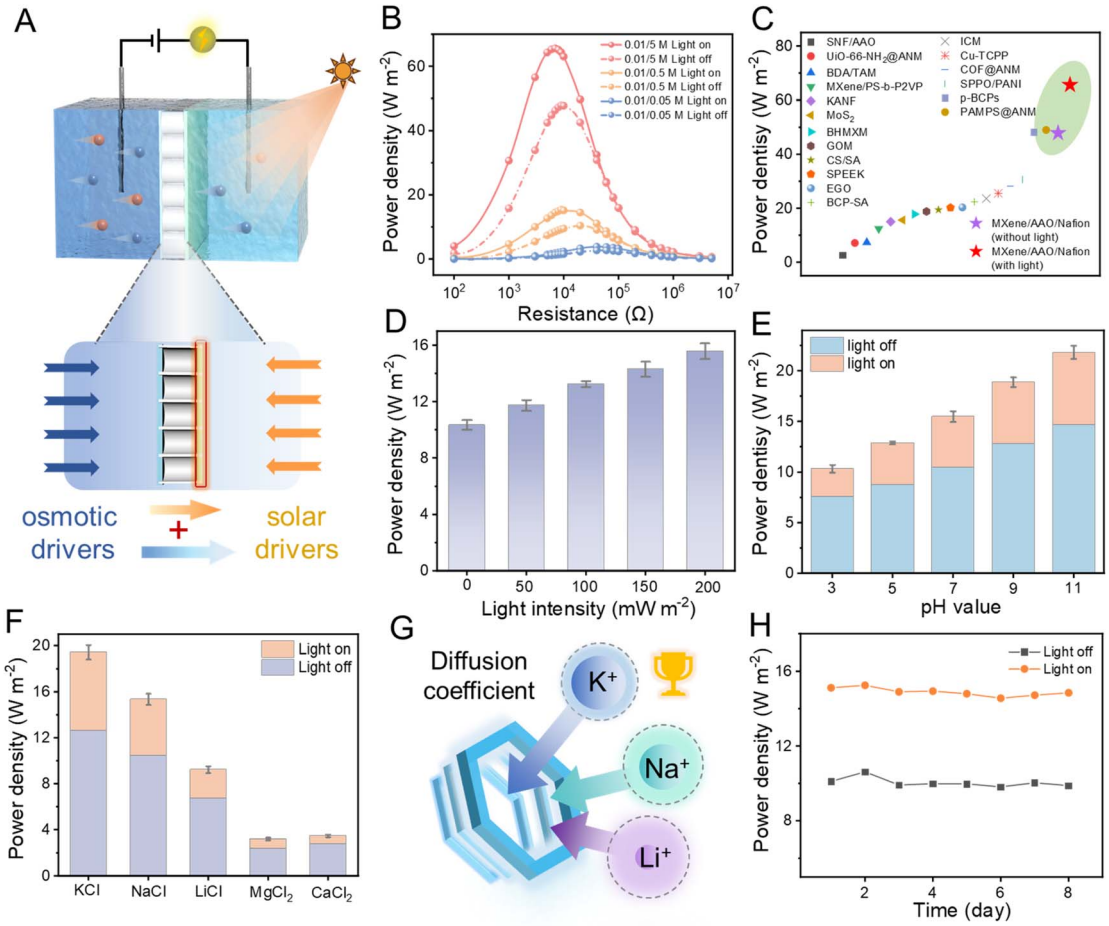

Fig. 5 Light-enhanced osmotic energy harvesting. (A) Schematic illustration of energy conversion with light irradiation. (B) Power density under a series of NaCl salinity gradients. (C) Comparison of the power density with previously reported devices at 500-fold NaCl salinity gradient. (D) Osmotic energy conversion performance at different light intensities. (E) Power density under different pH. (F) Power density under different electrolytes at 50-fold salinity gradient. (G) Schematic illustration of different cation electrolyte effects. (H) Testing the stability of the MXene/AAO/Nafion membrane in energy conversion.

the high-salinity environment (Fig. S44†). Moreover, under light illumination, the power density consistently maintained over 40% enhancement across all tested concentration gradients. Comparing performance, the MXene/AAO/Nafion membrane exceeds that of most of previously reported RED membranes (Fig. 5C and Table S5†).[7,15,39–55]

Many factors, such as light intensity, membrane area and pH value of electrolyte, can influence the performance of osmotic energy harvesting. First, the power density and current density of the MXene/AAO/Nafion membrane increase with the enhancement of light intensity (Fig. 5D and S45†). Furthermore, it has been observed that a smaller membrane area can lead to a higher output power density (Fig. S46†). Similar results have been achieved in previous works, which was mainly attributed to interfacial ICP regional coupling of parallel nanochannels in porous devices.[31] Despite the notably reduced power density compared to the small test area, the two-sided asymmetric MXene/AAO/Nafion membrane still exhibits the best performance after illumination compared to Nafion/AAO and Nafion/AAO/Nafion (Fig. S47–S50†). This can be attributed to the dual ion selective layer and improved permselectivity of the two-sided asymmetric structure, as well as the additional driving force for ion transport provided by the photothermal effect. Meanwhile, pH value also plays an important role in ion transport. As the pH value of the solution varies from 3.0 to 11.0, the output power density increases from 15.5 to 21.8 W m^{-2} under illumination (Fig. 5E and S51†), owing to the increased surface charge densities of MXene layer and Nafion layer.

Ion type is also important in practical osmotic energy harvest applications. We studied the output power of the MXene/AAO/Nafion membrane in various electrolyte systems (Fig. 5F and S52†). For different monovalent cation electrolyte solutions, KCl solution shows the highest power density of 19.5 W m^{-2} under illumination. However, in LiCl electrolyte under the same conditions, the maximum output power is only 9.2 W m^{-2}. Previous studies have demonstrated that the disparity in ion diffusion coefficients among various electrolytes accounts for this phenomenon, with greater coefficients enabling more effective charge separation.[15] The output power for monovalent cations (K^+ > Na^+ > Li^+) aligns precisely with their diffusion

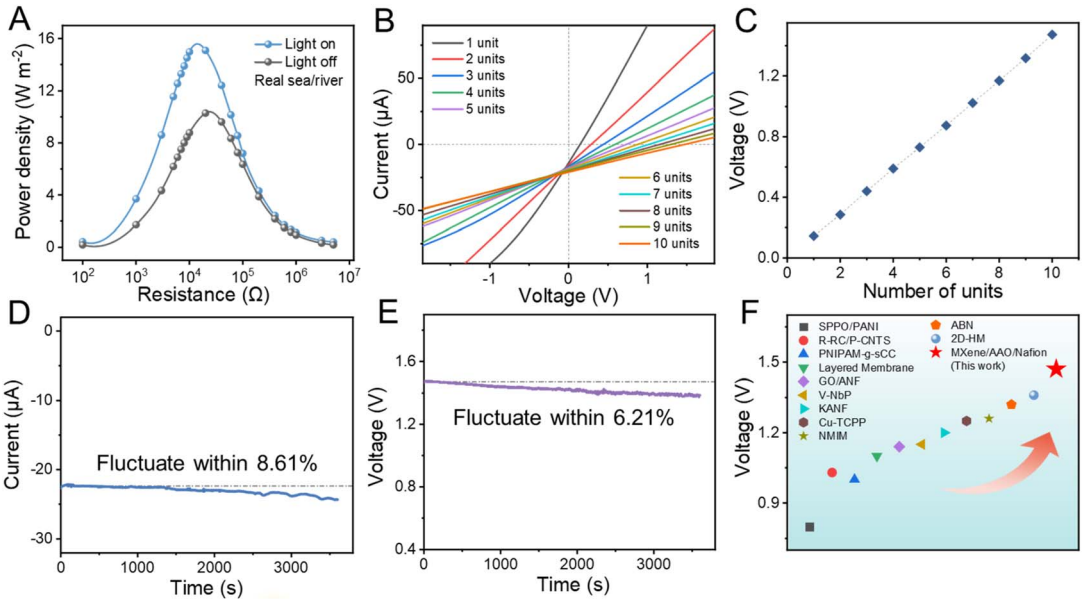

Fig. 6 Practical application of the MXene/AAO/Nafion membrane-based generator. (A) The energy conversion performance of the MXene/AAO/Nafion membrane for real river water/seawater conditions with and without light irradiation. (B) *I–V* curves of the MXene/AAO/Nafion power generators (from 1 to 10 units). (C) The relationship between the output voltage of a single generator and the number of generators. (D) The current and (E) voltage generated by a 10-unit generator operated continuously for over 1 h. (F) Comparison of the voltage of 10 units with that of previously reported devices.

coefficient ranking (Fig. 5G). Divalent cation solutions ($MgCl_2$, $CaCl_2$) produce lower power densities (~3.2 and 3.5 W m^{-2}) than monovalent electrolytes, primarily due to their decreased diffusion coefficients resulting from larger hydrated ionic sizes. In addition, the MXene/AAO/Nafion membrane retains 96% of its initial short-circuit current after 3600 s of continuous operation without renewing electrolyte (Fig. S53†). The output power exhibits remarkable stability even after a duration of 8 days, indicating the presented MXene/AAO/Nafion membrane has excellent long-term working stability (Fig. 5H and S54†).

Practical application prospects

To assess the practical applicability of the MXene/AAO/Nafion membrane, we examined its power density using natural Qingdao coastal seawater and river water (Fig. 6A). The measured output power density (10.3 W m^{-2}) closely matched the value obtained under a 0.01/0.5 M NaCl concentration gradient (10.4 W m^{-2}) and significantly exceeded the 5 W m^{-2} benchmark for commercial membranes. Moreover, the membrane maintained stable energy conversion performance and structural integrity even after 14 days of testing under real river water/seawater condition (Fig. S55–S58†). To further boost the application of osmotic energy conversion, we have developed a tandem MXene/AAO/Nafion membrane-based generator. Fig. 6B displays the *I–V* curves for 1 to 10 units of the generator subjected to a 50-fold NaCl salinity gradient. The output voltages demonstrate a linear relationship with the number of stacked units; 10 units of the generator can produce a voltage of 1.47 V (Fig. 6C). Without electrolyte replenishment, the output voltage obtained from a series of 10 units exhibits only a 6.21% attenuation over 1 h, accompanied by low attenuation in current, demonstrating that the MXene/AAO/Nafion membrane-based generator can continuously provide electric energy from osmotic energy (Fig. 6D, E). Under identical conditions, the MXene/AAO/Nafion membrane-based generator with 10 units achieves a higher output voltage compared to other reported membrane-based generators (Fig. 6F and Table S6†). Moreover, the tandem stacks of the generator have the capability of providing direct power for a wristwatch (Fig. S59 and S60†).

Conclusions

We have designed and prepared a kind of two-sided asymmetric MXene/AAO/Nafion membrane for enhanced ion transport and osmotic energy harvesting. Two functional layers with abundant negative surface charges on both sides of AAO realize a dual separation mechanism, where cations are initially rapidly separated in the Nafion layer, then followed by accelerated transport by the interface potential abruptness between AAO channels and the MXene layer. Benefiting from dual ion selectivity, a high cation selectivity and permeability can be achieved. Furthermore, the light-to-heat conversion efficiency of MXene also leads to a temperature gradient, achieving temperature-driven directional ion migration. The combination of concentration-driven and light-driven processes largely promotes the transmembrane ion transfer behavior. As a result, the present MXene/AAO/Nafion membrane displays exceptional performance for the salinity gradient power harvesting. The maximum output power density at 500-fold NaCl gradient concentration can reach up to approximately 65.6 W m^{-2}, which surpasses that of the majority of previously reported membranes (3.0–35.0 W m^{-2}). This work

indicates the importance of structure design in ion transport and its potential applications, providing a novel strategy for addressing global energy demands through high-performance blue energy harvesting.

Experimental

Materials and reagents

The aluminum foil used in this study was 0.1 mm thick with 99.999% purity, obtained from the General Research Institute for Non-ferrous Metals in Beijing, China. The chemicals used in this work, including tin(II) chloride ($SnCl_2$), potassium hydroxide (KOH), phosphoric acid (H_3PO_4), hydrogen peroxide (30% H_2O_2), chromium oxide (CrO_3) and acetic acid, were obtained from Sinopharm Chemical Reagent Co. Ltd (Shanghai, China). Magnesium chloride ($MgCl_2$), lithium chloride (LiCl), sodium chloride (NaCl), potassium chloride (KCl), calcium chloride ($CaCl_2$), acetone, and oxalic acid dihydrate were obtained from Shanghai Ling Feng Chemical Reagent Co. Ltd. Lithium fluoride (LiF) and *N*-methylpyrrolidone (NMP) were purchased from Aladdin. 5% Nafion 117 solution was obtained from Sigma-Aldrich. Ti_3AlC_2 was purchased from Shandong Research New Material Technology Co. Ltd. Ultrapure water was used in all the experiments.

Instrumentation

The morphological characteristics of the MXene/AAO/Nafion membrane were investigated using SEM (JSM-7600F, Japan). XPS (EscaLab Xi+, Thermo Fisher Scientific, USA) and XRD (Smart Lab) were used for the characterization of MXene ($Ti_3C_2T_x$). Zeta potential was measured using a Zetasizer Ultra. Water contact angle was determined with a fully automatic contact angle measuring instrument (DSA30S, Germany). All electrochemical tests were performed with a CHI660E electrochemical workstation (Shanghai Chenhua Instruments, China) using various electrolyte solutions.

Fabrication of AAO

AAO was prepared by a two-step anodizing method.[56] Initially, an aluminum plate was cleaned sequentially with acetone and 1 M KOH. During the first anodization process, 0.3 M $H_2C_2O_4$ was used as the electrolyte. A voltage of 50 V was applied, while magnetic stirring was maintained at 500 rpm for 30 min. Then, to obtain a well-ordered aluminum surface, the initially formed anodized layer was chemically etched using a mixed acid solution (5 wt% H_3PO_4 and 1.5 wt% H_2CrO_4) at 60 °C for 40 min. The second anodization was conducted for a duration of 4 h, following the same conditions as the initial anodization process. Afterwards, the prepared AAO membrane was treated with a $SnCl_2$ saturated solution to eliminate remaining aluminum residues. To remove the barrier layer, the AAO membrane was treated with a 5 wt% H_3PO_4 solution. Subsequently, the membrane was exposed to 30% H_2O_2 at boiling temperature for 30 min, which introduced numerous hydroxyl groups onto the channel surfaces.

Fabrication of $Ti_3C_2T_x$ MXene nanosheets

The detailed synthesis method was slightly modified from previous literature.[15] $Ti_3C_2T_x$ MXene was synthesized as follows. LiF (0.75 g) was dissolved in 10 mL of 9 M HCl using a 50 mL Teflon beaker. The solution was then supplemented with 0.5 g of Ti_3AlC_2 and stirred magnetically at 35 °C for 24 h. The obtained product was repeatedly washed with DI water and centrifuged at 3500 rpm until achieving a supernatant pH > 6, resulting in the formation of a sediment with clay-like characteristics. Subsequently, under conditions of 0 °C and an N_2 atmosphere, ultrasound was used to disperse the precipitate in deionized water for 60 min, facilitating the delamination of stacked MXene flakes. After centrifuging at 3500 rpm for 30 min, most of the unexfoliated MXene was removed. The prepared MXene solution was ~1 mg mL^{-1} in concentration. It was stored at 5 °C away from light.

Fabrication of the MXene/AAO/Nafion membrane

A 1 mg mL^{-1} MXene nanosheet dispersion was diluted with DI water to 0.01 mg mL^{-1}. Then, a certain volume of the dispersion was vacuum-filtered on one side of the AAO surface. Subsequently, it was heat-fixed in an oven at 80 °C for 6 h to obtain MXene/AAO. Different thicknesses of MXene layers can be obtained by varying the volume of dispersion used. Nafion dispersion was obtained by mixing 5% Nafion and NMP at 1 : 1. The Nafion dispersion was then spin-coated on the AAO side of MXene/AAO. The dispersion was spin-coated with 60 μL at a time, then with 500 rpm for 60 s and then with 1000 rpm for 120 s. The dispersion was then fixed in an oven at 45 °C for 24 h to afford the MXene/AAO/Nafion membrane.

Electrical measurement

The MXene/AAO/Nafion membrane was assembled between custom-fabricated electrochemical cell compartments, each filled with 2.5 mL electrolyte. Ion current signals were monitored *via* high-stability Ag/AgCl electrodes using a CHI660E electrochemical workstation.

The transmembrane voltage was adjusted within a certain range. These experiments were carried out using silica gel sheets measuring 0.2 mm in diameter. When the hybrid membrane is used to measure salinity gradient power generation, the effective experimental area is about 0.03 mm^2. The experiments were conducted at room temperature.

Data availability

The data supporting the findings can be found in the article and ESI,† and are available from the authors upon reasonable request.

Author contributions

Qijun Zheng: conceptualization, methodology, formal analysis, investigation, resources, data curation and writing. Yue Shen: formal analysis, investigation and resources. Junjian Lu: methodology and investigation. Yan Xu: conceptualization and

supervision. Xing-Hua Xia: conceptualization, supervision and project administration. Chen Wang: conceptualization, supervision, writing and project administration.

Conflicts of interest

There are no conflicts to declare.

Acknowledgements

This work was financially supported by the National Natural Science Foundation of China (22274076), the Primary Research & Development Plan of Jiangsu Province (BE2022793).

References

1 B. E. Logan and M. Elimelech, Membrane-based processes for sustainable power generation using water, *Nature*, 2012, **488**, 313–319.
2 G. Laucirica, M. E. Toimil-Molares, C. Trautmann, W. Marmisoll and O. Azzaroni, Nanofluidic osmotic power generators - advanced nanoporous membranes and nanochannels for blue energy harvesting, *Chem. Sci.*, 2021, **12**, 12874–12910.
3 Q. R. Liang, Y. N. Huang, Y. X. Guo, X. Zhang, X. M. Hu, H. Zeng, K. Liang, D. Y. Zhao, L. Jiang and B. Kong, Efficient osmosis-powered production of green hydrogen, *Nat. Sustain.*, 2024, **7**, 628–639.
4 L. Cao, I. C. Chen, X. W. Liu, Z. Li, Z. Y. Zhou and Z. P. Lai, An Ionic Diode Covalent Organic Framework Membrane for Efficient Osmotic Energy Conversion, *ACS Nano*, 2022, **16**, 18910–18920.
5 C. L. Chen, L. K. Meng, L. Cao, D. L. Zhang, S. H. An, L. M. Liu, J. J. Wang, G. X. Li, T. T. Pan, J. Shen, Z. J. Chen, Z. Shi, Z. P. Lai and Y. Han, Phase Engineering of Zirconium MOFs Enables Efficient Osmotic Energy Conversion: Structural Evolution Unveiled by Direct Imaging, *J. Am. Chem. Soc.*, 2024, **146**, 11855–11865.
6 J. Xiao, M. Y. Cong, M. M. Li, X. Zhang, Y. H. Zhang, X. J. Zhao, W. Q. Lu, Z. M. Guo, X. M. Liang and G. Y. Qing, Self-Assembled Nanoporous Metal-Organic Framework Monolayer Film for Osmotic Energy Harvesting, *Adv. Funct. Mater.*, 2023, **34**, 2307996.
7 K. R. Bang, C. Kwon, H. Lee, S. Kim and E. S. Cho, Horizontally Asymmetric Nanochannels of Graphene Oxide Membranes for Efficient Osmotic Energy Harvesting, *ACS Nano*, 2023, **17**, 10000–10009.
8 D. J. Wang, Z. Q. Wang, J. L. Chen, H. Zhi, Y. X. Liu, J. B. Tang, N. B. Li, Y. F. Zhang, M. An, H. Liu and G. B. Xue, Low-Friction Graphene Oxide-Based Ion Selective Membrane for High-Efficiency Osmotic Energy Harvesting, *Adv. Energy Mater.*, 2023, **14**, 2302262.
9 Z. Zhang, P. P. Zhang, S. Yang, T. Zhang, M. Löffler, H. H. Shi, M. R. Lohe and X. L. Feng, Oxidation promoted osmotic energy conversion in black phosphorus membranes, *Proc. Natl. Acad. Sci. U. S. A.*, 2020, **117**, 13959–13966.
10 Y. Hu, H. Y. Xiao, L. Fu, P. Liu, Y. D. Wu, W. P. Chen, Y. C. Qian, S. Y. Zhou, X. Y. Kong, Z. Zhang, L. Jiang and L. P. Wen, Confined Ionic-Liquid-Mediated Cation Diffusion through Layered Membranes for High-Performance Osmotic Energy Conversion, *Adv. Mater.*, 2023, **35**, 2301285.
11 A. Awati, R. Yang, T. Shi, S. Zhou, X. Zhang, H. Zeng, Y. K. Lv, K. Liang, L. Xie, D. Z. Zhu, M. X. Liu and B. Kong, Interfacial Supe-Assembly of Vacancy Engineered Ultrathin-Nanosheets Toward Nanochannels for Smart Ion Transport and Salinity Gradient Power Conversion, *Angew. Chem., Int. Ed.*, 2024, **63**, e202407491.
12 J. Safaei, Y. F. Gao, M. Hosseinpour, X. Y. Zhang, Y. Sun, X. Tang, Z. J. Zhang, S. J. Wang, X. Guo, Y. Wang, Z. Chen, D. Zhou, F. Y. Kang, L. Jiang and G. X. Wang, Vacancy Engineering for High-Efficiency Nanofluidic Osmotic Energy Generation, *J. Am. Chem. Soc.*, 2023, **145**, 2669–2678.
13 P. Liu, T. Zhou, L. S. Yang, X. Li, L. Jiang and L. P. Wen, Harvesting ionic power from a neutralization reaction through a heterogeneous graphene oxide membrane, *Chem. Sci.*, 2025, **16**, 1857–1866.
14 M. Rastgar, K. Moradi, C. Burroughs, A. Hemmati, E. Hoek and M. Sadrzadeh, Harvesting Blue Energy Based on Salinity and Temperature Gradient: Challenges, Solutions, and Opportunities, *Chem. Rev.*, 2023, **123**, 10156–10205.
15 L. Ding, M. Zheng, D. Xiao, Z. Zhao, J. Xue, S. Zhang, J. Caro and H. Wang, Bioinspired $Ti_3C_2T_x$ MXene-Based Ionic Diode Membrane for High-Efficient Osmotic Energy Conversion, *Angew. Chem., Int. Ed.*, 2022, **61**, e202206152.
16 C. W. Chu, A. R. Fauziah and L. H. Yeh, Optimizing Membranes for Osmotic Power Generation, *Angew. Chem., Int. Ed.*, 2023, **62**, e202303582.
17 J. R. Hao, B. Bao, J. J. Zhou, Y. S. Cui, X. C. Chen, J. L. Zhou, Y. H. Zhou and L. Jiang, A Euryhaline-Fish-Inspired Salinity Self-Adaptive Nanofluidic Diode Leads to High-Performance Blue Energy Harvesters, *Adv. Mater.*, 2022, **34**, 2203109.
18 J. Wang, Z. Cui, S. Z. Li, Z. Y. Song, M. L. He, D. X. Huang, Y. Feng, Y. Z. Liu, K. Zhou, X. D. Wang and L. Wang, Unlocking osmotic energy harvesting potential in challenging real-world hypersaline environments through vermiculite-based hetero-nanochannels, *Nat. Commun.*, 2024, **15**, 608.
19 Y. M. Guo, X. Sun, S. S. Ding, J. Lu, H. T. Wang, Y. Zhu and L. Jiang, Charge-Gradient Sulfonated Poly(ether ether ketone) Membrane with Enhanced Ion Selectivity for Osmotic Energy Conversion, *ACS Nano*, 2024, **18**, 7161–7169.
20 M. Abdollahzadeh, M. Chai, E. Hosseini, M. Zakertabrizi, M. Mohammad, H. Ahmadi, J. W. Hou, S. Lim, A. H. Korayem, V. Chen, M. Asadnia and A. Razmjou, Designing Angstrom-Scale Asymmetric MOF-on-MOF Cavities for High Monovalent Ion Selectivity, *Adv. Mater.*, 2022, **34**, 2107878.
21 Z. Q. Li, G. L. Zhu, R. J. Mo, M. Y. Wu, X. L. Ding, L. Q. Huang, Z. Q. Wu and X. H. Xia, Janus Metal-Organic Framework Membranes Boosting the Osmotic Energy Harvesting, *ACS Appl. Mater.*, 2023, **15**, 23922–23930.

22 B. W. Lv, S. Li, W. Wang, Y. L. Xu, B. G. Zhao, C. W. Song, X. F. Fan and Y. M. Liu, A lotus leaf-inspired Janus dual-functional nanofiber evaporator for efficient water purification, *J. Clean. Prod.*, 2024, **438**, 140880.

23 C. C. Zhu, L. Xu, Y. Z. Liu, J. Liu, J. Wang, H. J. Sun, Y. Q. Lan and C. Wang, Polyoxometalate-based plasmonic electron sponge membrane for nanofluidic osmotic energy conversion, *Nat. Commun.*, 2024, **15**, 4213.

24 Z. J. Yang, L. H. Yeh, Y. H. Peng, Y. P. Chuang and K. C. W. Wu, Enhancing Ionic Selectivity and Osmotic Energy by Using an Ultrathin Zr-MOF-Based Heterogeneous Membrane with Trilayered Continuous Porous Structure, *Angew. Chem., Int. Ed.*, 2024, **63**, e202408375.

25 L. Liu, H. C. Lan, Y. Q. T. Cui, Q. Wen, J. Q. Bai, X. Q. An, M. Sun, H. J. Liu and J. H. Qu, A Janus membrane with electro-induced multi-affinity interfaces for high- efficiency water purification, *Sci. Adv.*, 2024, **10**, 8696.

26 X. Li, Z. L. Wang and D. Wei, Scavenging Energy and Information through Dynamically Regulating the Electrical Double Layer, *Adv. Funct. Mater.*, 2024, **34**, 2405520.

27 S. Hong, G. Zou, H. Kim, D. Huang, P. Wang and H. N. Alshareef, Photothermoelectric Response of Ti3C2Tx MXene Confined Ion Channels, *ACS Nano*, 2020, **14**, 9042–9049.

28 X. F. Wang, X. Shen, Y. R. Gao, Z. X. Wang, R. C. Yu and L. Q. Chen, Atomic-Scale Recognition of Surface Structure and Intercalation Mechanism of Ti3C2X, *J. Am. Chem. Soc.*, 2015, **137**, 2715–2721.

29 F. I. Allen, L. R. Comolli, A. Kusoglu, M. A. Modestino, A. M. Minor and A. Z. Weber, Morphology of Hydrated As-Cast Nafion Revealed through Cryo Electron Tomography, *ACS Macro Lett.*, 2014, **4**, 1–5.

30 X. Tong, S. Liu, J. Crittenden and Y. S. Chen, Nanofluidic Membranes to Address the Challenges of Salinity Gradient Power Harvesting, *ACS Nano*, 2021, **15**, 5838–5860.

31 S. Zhou, L. Xie, X. Zhang, M. Yan, H. Zeng, K. Liang, L. Jiang and B. Kong, Super-Assembled Multi-Level Asymmetric Mesochannels for Coupled Accelerated Dual-Ion Selective Transport, *Adv. Mater.*, 2022, **35**, 2208903.

32 Z. D. Hao, C. J. Wang, Y. Wu, Q. Q. Zhang, H. Xu, Y. H. Jin, J. B. Liu, H. Wang and X. M. He, Electronegative Nanochannels Accelerating Lithium-Ion Transport for Enabling Highly Stable and High-Rate Lithium Metal Anodes, *Adv. Energy Mater.*, 2023, **13**, 2204007.

33 Y. H. Zhang, L. L. Wang, Q. Bian, C. C. Zhong, Y. P. Chen and L. Jiang, Enhanced Ionic Power Generation via Light-Driven Active Ion Transport Across 2D Semiconductor Heterostructures, *Small*, 2024, **20**, 2311379.

34 C.-W. Chang, C.-W. Chu, Y.-S. Su and L.-H. Yeh, Space charge enhanced ion transport in heterogeneous polyelectrolyte/alumina nanochannel membranes for high-performance osmotic energy conversion, *J. Mater. Chem. A*, 2022, **10**, 2867–2875.

35 C. J. Zhu, X. H. Zuo, W. P. Xian, Q. Guo, Q. W. Meng, S. Wang, S. Q. Ma and Q. Sun, Integration of Thermoelectric Conversion with Reverse Electrodialysis for Mitigating Ion Concentration Polarization and Achieving Enhanced Output Power Density, *ACS Energy Lett.*, 2022, **7**, 2937–2943.

36 X. H. Zuo, C. J. Zhu, W. P. Xian, Q. W. Meng, Q. Guo, X. C. Zhu, S. Wang, Y. Q. Wang, S. Q. Ma and Q. Sun, Thermo-Osmotic Energy Conversion Enabled by Covalent-Organic-Framework Membranes with Record Output Power Density, *Angew. Chem., Int. Ed.*, 2022, **61**, e202116910.

37 P. Liu, T. Zhou, Y. F. Teng, L. Fu, Y. H. Hu, X. B. Lin, X. Y. Kong, L. Jiang and L. P. Wen, Light-Induced Heat Driving Active Ion Transport Based on 2D MXene Nanofluids for Enhancing Osmotic Energy Conversion, *CCS Chem.*, 2021, **3**, 1325–1335.

38 J. Wang, C. Wang, J.-J. Xu, X.-H. Xia and H.-Y. Chen, Emerging advances in plasmonic nanoassemblies for biosensing and cell imaging, *Chin. Chem. Lett.*, 2023, **34**, 108165.

39 J. Wang, Z. Y. Song, M. L. He, Y. C. Qian, D. Wang, Z. Cui, Y. Feng, S. Z. Li, B. Huang, X. Y. Kong, J. M. Han and L. Wang, Light-responsive and ultrapermeable two-dimensional metal-organic framework membrane for efficient ionic energy harvesting, *Nat. Commun.*, 2024, **15**, 2125.

40 W. W. Xin, Z. Zhang, X. D. Huang, Y. H. Hu, T. Zhou, C. C. Zhu, X. Y. Kong, L. Jiang and L. P. Wen, High-performance silk-based hybrid membranes employed for osmotic energy conversion, *Nat. Commun.*, 2019, **10**, 3876.

41 Y. C. Liu, L. H. Yeh, M. J. Zheng and K. C. W. Wu, Highly selective and high-performance osmotic power generators in subnanochannel membranes enabled by metal-organic frameworks, *Sci. Adv.*, 2021, **7**, eabe9924.

42 C. Wang, J. D. Tang, L. Y. Li, J. H. Wan, Y. C. Ma, Y. H. Jin, J. B. Liu, H. Wang and Q. Q. Zhang, Ultrathin Self-Standing Covalent Organic Frameworks toward Highly-Efficient Nanofluidic Osmotic Energy Generator, *Adv. Funct. Mater.*, 2022, **32**, 2204068.

43 X. B. Lin, P. Liu, W. W. Xin, Y. F. Teng, J. J. Chen, Y. D. Wu, Y. F. Zhao, X. Y. Kong, L. Jiang and L. P. Wen, Heterogeneous MXene/PS-b-P2VP Nanofluidic Membranes with Controllable Ion Transport for Osmotic Energy Conversion, *Adv. Funct. Mater.*, 2021, **31**, 2105013.

44 L. Ding, D. Xiao, Z. H. Zhao, Y. Y. Wei, J. Xue and H. H. Wang, Ultrathin and Ultrastrong Kevlar Aramid Nanofiber Membranes for Highly Stable Osmotic Energy Conversion, *Adv. Sci.*, 2022, **9**, 2202869.

45 C. C. Zhu, P. Liu, B. Niu, Y. N. Liu, W. W. Xin, W. P. Chen, X. Y. Kong, Z. Zhang, L. Jiang and L. P. Wen, Metallic Two-Dimensional MoS_2 Composites as High-Performance Osmotic Energy Conversion Membranes, *J. Am. Chem. Soc.*, 2021, **143**, 1932–1940.

46 Y. J. Qian, D. Liu, G. L. Yang, L. F. Wang, Y. C. Liu, C. Chen, X. G. Wang and W. W. Lei, Boosting Osmotic Energy Conversion of Graphene Oxide Membranes via Self-Exfoliation Behavior in Nano-Confinement Spaces, *J. Am. Chem. Soc.*, 2022, **144**, 13764–13772.

47 G. S. Bian, N. Pan, Z. H. Luan, X. Sui, W. X. Fan, Y. Z. Xia, K. Y. Sui and L. Jiang, Anti-Swelling Gradient

Polyelectrolyte Hydrogel Membranes as High-Performance Osmotic Energy Generators, *Angew. Chem., Int. Ed.*, 2021, **60**, 20294–20300.

48 Y. Y. Zhao, J. Wang, X. Y. Kong, W. W. Xin, T. Zhou, Y. C. Qian, L. S. Yang, J. H. Pang, L. Jiang and L. P. Wen, Robust sulfonated poly (ether ether ketone) nanochannels for high-performance osmotic energy conversion, *Natl. Sci. Rev.*, 2020, **7**, 1349–1359.

49 C. Li, L. P. Wen, X. Sui, Y. R. Cheng, L. C. Gao and L. Jiang, Large-scale, robust mushroom-shaped nanochannel array membrane for ultrahigh osmotic energy conversion, *Sci. Adv.*, 2021, **7**, eabg2183.

50 W. P. Chen, T. D. Dong, Y. Xiang, Y. C. Qian, X. L. Zhao, W. W. Xin, X. Y. Kong, L. Jiang and L. P. Wen, Ionic Crosslinking-Induced Nanochannels: Nanophase Separation for Ion Transport Promotion, *Adv. Mater.*, 2021, **34**, 2108410.

51 M. Y. Gao, M.-J. Zheng, A. F. M. El-Mahdy, C.-W. Chang, Y.-C. Su, W.-H. Hung, S.-W. Kuo and L.-H. Yeh, A bioinspired ionic diode membrane based on sub-2 nm covalent organic framework channels for ultrahigh osmotic energy generation, *Nano Energy*, 2023, **105**, 108007.

52 X. Y. Zhang, B. H. Wu, H. Q. Wu and P. Y. Wu, Engineering Multiscale Heterostructure as Ionic Diode and Light-Driven Ion Pump for Osmotic-Solar Energy Harvesting, *CCS Chem.*, 2025, **7**, 1383–1395.

53 C. Li, H. M. Jiang, P. X. Liu, Y. Zhai, X. Q. Yang, L. C. Gao and L. Jiang, One Porphyrin Per Chain Self-Assembled Helical Ion-Exchange Channels for Ultrahigh Osmotic Energy Conversion, *J. Am. Chem. Soc.*, 2022, **144**, 9472–9478.

54 Y.-C. Lin, H.-H. Chen, C.-W. Chu and L.-H. Yeh, Massively Enhanced Charge Selectivity, Ion Transport, and Osmotic Energy Conversion by Antiswelling Nanoconfined Hydrogels, *Nano Lett.*, 2024, **24**, 11756–11762.

55 W.-H. Lin, T.-Y. Huang, C.-H. Bai, C.-H. Hung, C.-A. Lung, W.-H. Hung, K. Gopinadhan and L.-H. Yeh, Novel ultrastable 2D MOF/MXene nanofluidic membrane with ultralow resistance for highly efficient osmotic power harvesting, *Nano Energy*, 2024, **128**, 109924.

56 J. H. Yuan, F. Y. He, D. C. Sun and X. H. Xia, A Simple Method for Preparation of Through-Hole Porous Anodic Alumina Membrane, *Chem. Mater.*, 2004, **16**, 1841–1844.